Summary of Doctoral Dissertation

Gold Nanoparticles as Injectable and Minimally Invasive Markers for Real-Time Image Guided Radiation Therapy

画像誘導放射線治療用の注射可能な低侵襲金ナノ粒子マーカー

LIU Haoran

Background and Objectives

Radiation therapy is one of the most cost-effective and prevalent modalities in cancer treatments,[1] as about 50% of patients will receive radiation therapy after diagnosis,[2] but it only accounts for only 5% of the total cost for cancer therapy.[3,4] The therapeutic effect of radiation therapy is highly dependent on the coverage of the targets with therapeutic dose and therefore one of the main challenges in radiation therapy is pinpointing the exact location and shape of tumors.[5] However, tumors rarely display a permanent position during irradiation due to breathing motion, peristalsis, and other body motions.[6] A larger three-dimensional planning margin is then required to compensate for the geometric and setup uncertainties, but it also brings increased exposure of normal tissue to radiation.[7]

Image-guided radiation therapy (IGRT) has accordingly emerged for optimizing therapeutic efficacy and minimizing treatment toxicity by improving the radiation delivery accuracy and lowering the dosage to nearby tissues or organs.[8,9] In IGRT techniques, internal reference points with a fixed position like a skeleton are normally necessary to clearly track the tumors. However, in some cases, the positions of tumors cannot be correlated with natural reference points, and fiducial markers are accordingly needed for high tumor positioning accuracy and precise dose delivery.

Fiducial markers are objects that are designed to be implanted in or close to tumors to serve as reference points. They are generally made of metal and have relatively large physical dimensions. The implantations of these fiducial markers with complicated insertion procedures are exceedingly invasive and may induce unfavorable complications on patients, such as pneumothorax,[10-12] infection,[13,14] and bleeding.

Gold is a kind of remarkable multimodal imaging agent for X-ray imaging,[15] computed tomography (CT) scan,[16,17] magnetic resonance imaging (MRI),[18] sonography,[19] photoacoustic (PA) imaging[20] owing to its electron density, unique optical properties, easy engineering in its shape and size, excellent biocompatibility, and stability *in vivo*. Apart from being an imaging agent, gold could be also used as therapeutic agents for photothermal therapy[21-23] and photodynamic therapy[24-26] if necessary. Gold is hence an ideal candidate for fiducial markers for IGRT. For the versatility of possible injection methods, small-sized gold at the nanoscale such as gold nanoparticles (Au NPs) is preferred in injection applications.

Therefore, this study aims to synthesize Au NPs via green, effective, and biocompatible methods for fiducial marker applications to achieve optimal therapeutic efficacy and minimal treatment toxicity, including:

a. Synthesizing Au NPs using the microwave-induced plasma-in-liquid process (MWPLP) with the addition of alginate for long-term storage of Au NPs;

b. Synthesizing Au NPs via a green ethanol reduction method with the addition of alginate to improve the reducing capacity of the ethanol system and the stability of the synthesized Au NPs;

c. Evaluating the potentials of Au NPs as injectable and minimally invasive fiducial markers based on their injectability and imaging performance;

d. Developing a ready-to-use injectable fiducial marker based on the synthesized Au NPs and a body temperature-activated *in situ* gel-forming system to ensure its long-term retaining *in vivo*, as well as to avoid its movement or Au NPs leakage *in vivo*.

Experimental Methods

1. Synthesis of alginate stabilized-Au NPs (alg-Au NPs) using the MWPLP

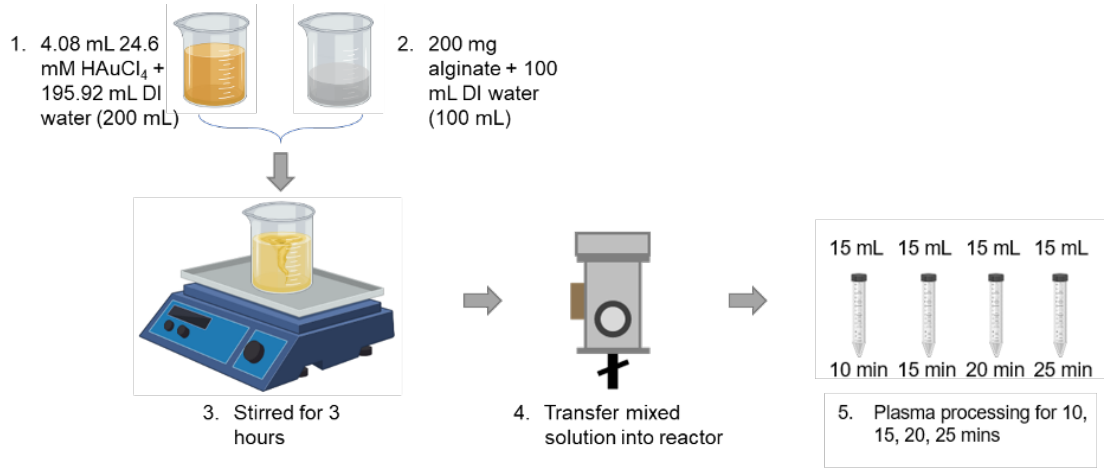

Scheme 1. Fabrication route for synthesizing Au NPs in aqueous solutions of sodium alginate and $AuCl_4^-$

The synthesis route is illustrated in Scheme 1. Sodium alginate solutions were prepared by dissolving sodium alginate into water and then mixed with $HAuCl_4$ solution at certain volume ratios. The mixed solution was stirred for 3 h for getting homogeneous solutions and then introduced into the reaction vessel. The microwave output was kept at 500 W during the reaction. The reaction lasted for different reaction times.

2. Synthesis of Au NPs via ethanol reduction method

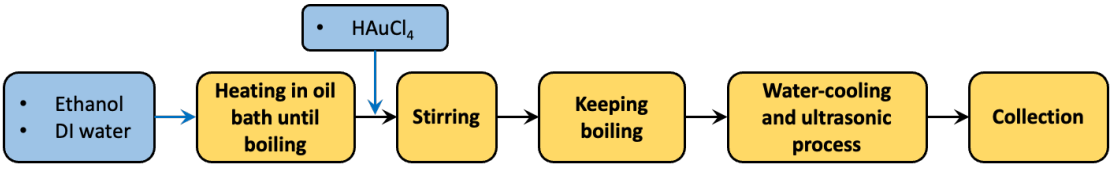

Scheme 2. Fabrication route for synthesizing Au NPs via ethanol reduction method

As shown in Scheme 2, to synthesize Au NPs, pure water and 200 mL ethanol were mixed into a 1 L two-necked flask and were heated in an oil bath. 8.1 mL aqueous solution of $HAuCl_4$ (24.6 mM) was added when the mixed solution boiled. The reaction solution was kept for 2 h under reflux and stirring at 800 rpm. When the reaction was completed, the products were collected after a 10-minute water-cooling and ultrasonic process. In order to synthesize alg-Au NPs, pure water was

replaced with an equal volume of sodium alginate aqueous solution and the concentrations of original sodium alginate aqueous solutions were 0.1, 0.5, and 1.0% w/v. The obtained alg-Au NPs were labelled with the original alginate concentrations: 0.1, 0.5, and 1.0% w/v.

3. Preparation of sodium alginate stabilized-Au NPs and GDL/$CaCO_3$/alg-Au NPs.

Liquid alg-Au NPs were dried with evaporator and vacuum and the obtained alg-Au NP powder was grinded with $CaCO_3$. The well-mixed powder was redispersed by pure water and mixed with glucono delta lactone (GDL) solution. The preparation of GDL solution and following mixing of GDL and powder were operated at a low temperature (ice bath) to avoid unexpected hydrolysis of GDL.

4. Characterization

A UV-Vis spectrophotometer (UV-1800, Shimadzu, Japan) was used for recording UV-Vis spectra of alg-Au NPs. The morphology and size of alg-Au NPs were characterized with a transmission electron microscopy (TEM, JEOL JEM 2000-FX, at 200 kV). Alg-Au NPs dispersion was dropped onto copper grids coated with collodion film and kept to dry naturally for preparing TEM samples. The thermal decomposition behavior of alg-Au NPs and GDL/$CaCO_3$/alg-Au NPs were evaluated on a thermogravimetric analyze (TG, DTA-60H, Shimadzu). To obtain storage and loss moduli of GDL/$CaCO_3$/alg and GDL/$CaCO_3$/alg-Au NPs, the rheological measurements were carried out on a TA Instruments ARES-G2 rheometer, using a cone and plate geometry with diameter D = 50 mm, cone angel = 0.04 rad, and gap d = 1.159 mm. Time sweep measurements were conducted at a strain amplitude of 1% and angular frequency of 1 rad/s at 4 or 37 °C. The injectability of GDL/$CaCO_3$/alg and GDL/$CaCO_3$/alg-Au NPs were tested on a universal load testing machine (JSV H1000, Algol Instrument) with fixed force mode and fixed displacement mode. Briefly, syringe (1 mL) with 21G and 25G needles, of which inner diameters are 0.51 mm and 0.26 mm, were used for loading samples. Fifty newton (surgeons' force during injection) force was applied on syringe to extrude samples. Injectability was defined as the volume proportion of the injected sample to the whole sample. The injectability under 50 N can be evaluated via fixed force mode, while the minimum force required for injecting all samples can be measured via fixed displacement mode. X-ray visualization test was carried out at the Central Institute of Isotope Science, Hokkaido University to assess the visibility of GDL/$CaCO_3$/alg-Au NPs. The samples were injected into jelly and the gelated samples were taken out for following X-ray visualization test. Samples were exposed to an X-ray tube (UD-150-B40, Shimadzu Corporation). A Flat Panel Detector (PaxScan 3030, Varian Medical System) was used to capture and record the X-rays that passed through the developed markers. To mimic the impact of body tissue on sample visibility, acrylic resins with an X-ray attenuation property comparable to that of the human body were positioned between the samples and the detector. Pattern matching scores calculated based on the images acquired by the detector were used for assessing the visibility of samples.

Results and Discussion

1. Synthesis of alg-Au NPs using MWPLP

In Chapter 2, alg-Au NPs using MWPLP were prepared. The introduction of alginate could (1) accelerate the reaction rate, (2) prevent aggregation and deposition due to long time discharge in MWPLP (Figure 1. (a)), and (3) provide long-term stability. The size of Au NPs prepared in different

concentrations of alginate ranged from 41 to 12 nm, indicating that the concentration of alginate could be used for controlling the size of Au NPs (Figure 1. (c)). An abnormal size change (from large to small) that is opposite to the typical particle growth in the bottom-up chemical reduction was observed. A possible mechanism of the observed phenomenon was proposed based on dynamical and thermodynamical instability (Figure 1. (d)). The alginate dispersions with Au NPs were dried and redispersed to evaluate the effect of the drying and redispersion process on the Au NPs. Results suggest that the process had an imperceptible effect on the Au NPs in terms of their size and dispersibility (Figure 2). Consequently, this strategy might be an effective technique for the long-term storage of Au NPs and other metal NPs. The stabilized Au NPs without the addition of toxic reducing or stabilizing agents can be appropriate for biomedical applications.

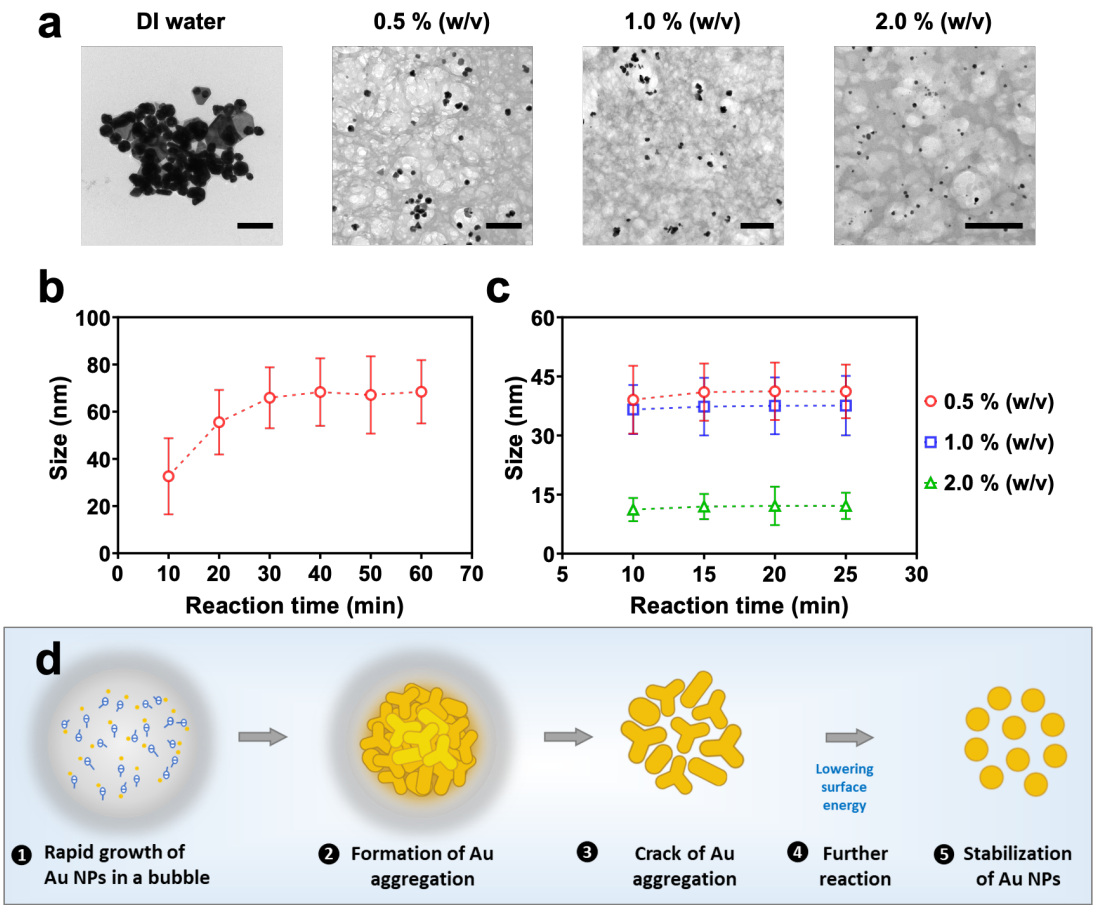

Figure 1. (a) TEM images of Au NPs prepared in pure water and sodium alginate aqueous solutions (reaction time: 20 min). Scale bars are 200 nm. (b) Average size of Au NPs prepared in pure water with different reaction times. (c) Average size of Au NPs prepared in alginate aqueous solution with different concentrations and reaction times. (d) Mechanism of alg-Au NP formation using MWPLP.

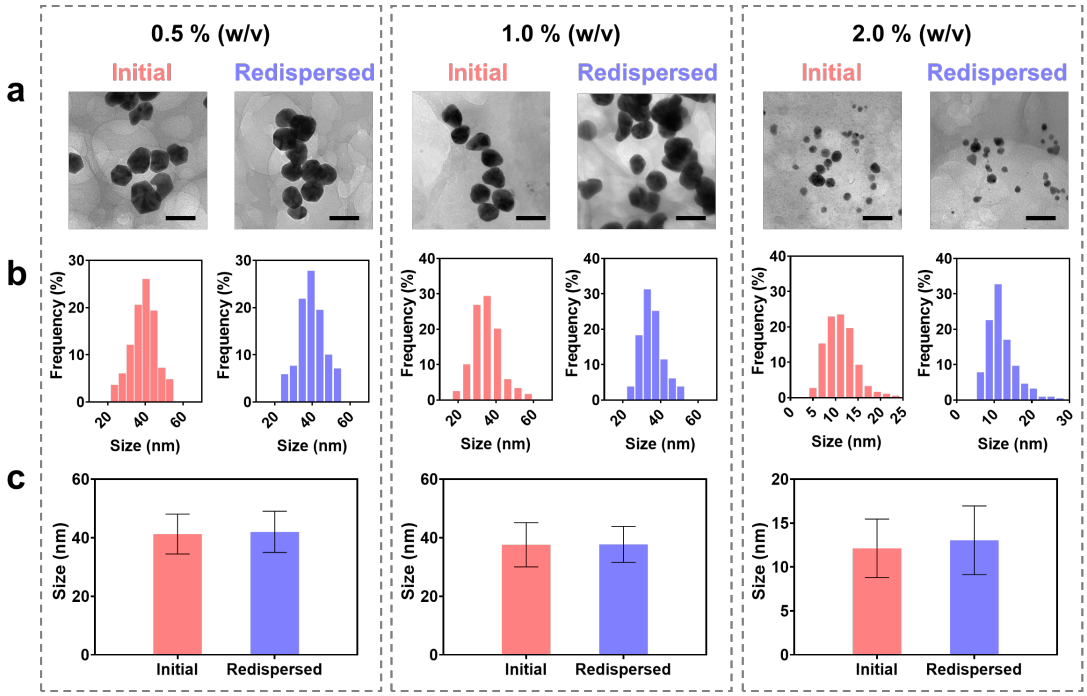

Figure 2. (a) TEM images, (b) size distributions, and (c) average sizes of Au NPs before drying and after redispersion with various sodium alginate concentrations. Scale bars, 50 nm.

2. Synthesis of Au NPs via ethanol reduction method

As plasma devices are only available at very few universities and institutes, ethanol reduction method, a more universal synthesis method, was explored for the preparation of Au NPs. Au NPs designed as injectable fiducial markers for IGRT were synthesized via ethanol-only and ethanol/alginate systems in Chapter 3. Their injectability and imaging capabilities as fiducial markers were evaluated. Within the range of parameters studied, injection medium viscosity, Au NPs concentration, needles gauge was found to be the major factors that would affect their injectability, while the gold amount and particle size dominated their imaging performance. Compared to conventional gold ball markers (1.5 or 2.0 mmφ), Au NPs synthesized in the ethanol-only system had an improved injectability (through 18G and 21G needles) and an almost identical imaging capability. This chapter also reports a novel reducing system based on the mixture of ethanol and alginate. The addition of alginate into the ethanol reduction system can improve the reaction efficiency, control the size of synthesized Au NPs, and prevent aggregation between Au NPs. As an anionic polymer with high charge density, alginate can significantly enhance the reducing capacity of the ethanol system and control the size of alg-Au NPs through the formed cavities and the increased nucleation probability. Due to the size control during synthesis, the alg-Au NPs with smaller sizes (14.1 to 21.8 nm) exhibited a superior injectability, up to 100% even through 25G needles with extrusion force less than 17 N (Figure 3. (a) and (b)), especially for the injection of high-concentration Au NPs. A better imaging capability of alg-Au NPs was also verified in the X-ray visualization test (Figure 3. (c)). Though the imaging performance of Au NPs and alg-Au NPs as fiducial markers has been examined and confirmed after injection.

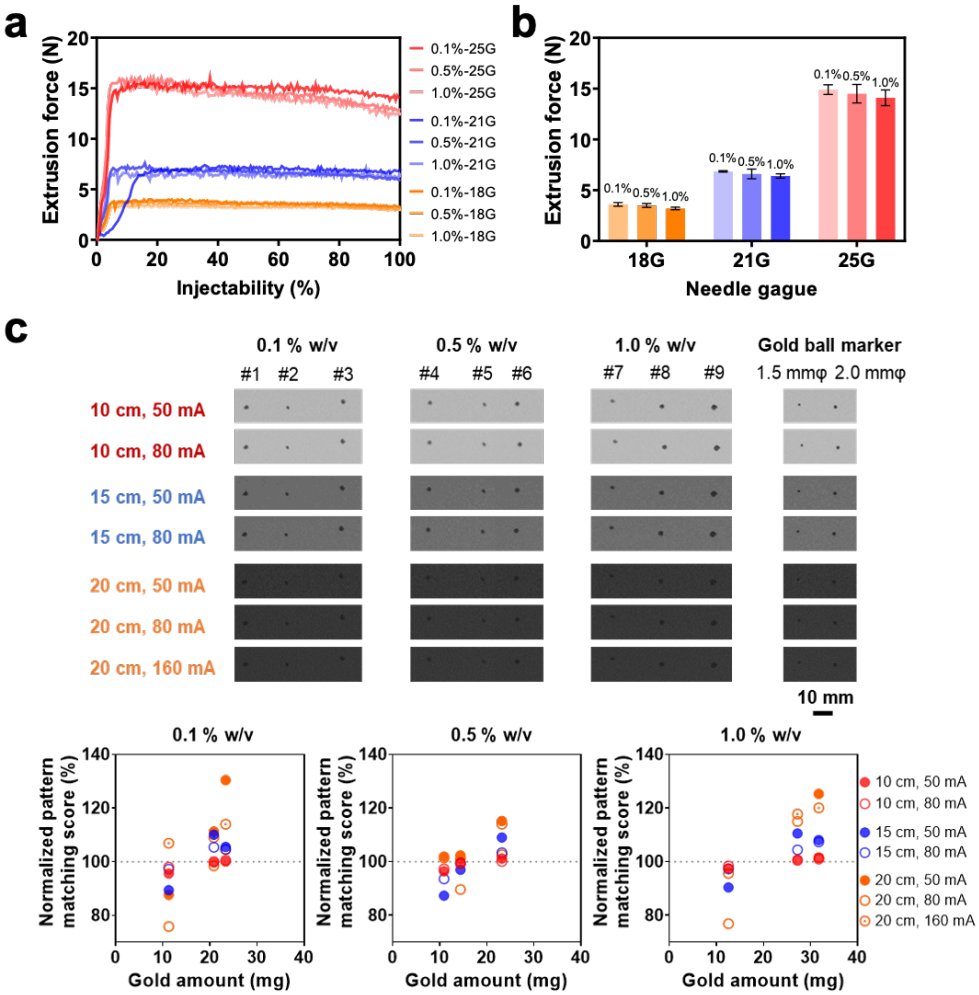

Figure 3. (a) Extrusion force curves and (b) average extrusion force of alg-Au NPs synthesized in different alginate concentrations through different needles. (c) X-ray visualization image of alg-Au NPs and gold ball markers under different acrylic resin thicknesses and tube currents, and relationship between normalized pattern matching scores and different gold amounts.

3. Development of a ready-to-use injectable marker based on the synthesized alg-Au NPs

In chapter 4, an injectable fiducial marker based on alg-Au NPs and a body temperature-activated *in situ* gel-forming system has been developed. Gram-scale Au NPs were prepared by the MWPLP in an hour. The addition of alginate could effectively stabilize a large amount of Au NPs and prevent their aggregation via the cavities formed by alginate chains. The body temperature-activated *in situ* gel-forming system GDL/$CaCO_3$/alg was designed based on the mild gelation ability of alginate with divalent cations and the temperature-dependent release of calcium source. GDL/$CaCO_3$/alg-Au NPs could maintain a liquid state when stored at low temperature due to the slow hydrolysis of GDL and release of Ca^{2+}. The hydrolysis of GDL could be activated and accelerated by body temperature after injection, resulting in the *in situ* formation of alginate gel. This nature allows for excellent injectability and stability of GDL/$CaCO_3$/alg-Au NPs at the storage temperature, and the capability of transforming into gel to fix Au NPs at the target site for an improved geometric accuracy, making it a ready-to-use injectable fiducial marker that is convenient for surgeons and minimally invasive for patients.

Conclusions and Perspectives

This study explores two strategies for the green, effective, and biocompatible synthesis of Au NPs and evaluates the potential of the synthesized Au NPs as injectable and minimally invasive fiducial markers. A ready-to-use injectable fiducial marker is developed for IGRT based on the synthesized Au NPs and a body temperature-activated *in situ* gel-forming system. The key results and conclusions are summarized as follows:

a. Chapter 2 describes the synthesis of alg-Au NPs using MWPLP. The synthesis of alg-Au NPs without using toxic reducing or stabilizing agents renders them appropriate for biomedical applications.
b. Chapter 3 presents the Au NPs synthesized via ethanol-only and ethanol/alginate systems. Their injectability and imaging capabilities as fiducial markers were evaluated.
c. Chapter 4 focuses on the development of a ready-to-use injectable fiducial marker, GDL/$CaCO_3$/alg-Au NPs, based on the synthesized alg-Au NPs and a body temperature-activated in situ gel-forming system.

As this injectable fiducial marker is designed to be used in humans' body during IGRT, attention should also be paid to its biological evaluation in subsequent work:

a. *in vitro* evaluations: cytotoxicity, degradation, cellular uptake, and apoptosis
b. *in vivo* evaluations: injectability, acute toxicity, stability, distribution, metabolism, imaging performance
c. other potential functions: radiosensitization, photothermal conversion

References

1. Baskar, R.; Lee, K. A.; Yeo, R.; Yeoh, K.W. Cancer and radiation therapy: current advances and future directions, Int. J. Med. Sci., 2012, 9, 193.
2. Delaney, G.; Jacob, S.; Featherstone, C.; Barton, M. The role of radiotherapy in cancer treatment: estimating optimal utilization from a review of evidence-based clinical guidelines, Cancer: Interdisciplinary, Int. J. Amer. Cancer Soc., 2005, 104, 1129-1137.
3. Ringborg, U.; Bergqvist, D.; Brorsson, B.; Cavallin-Ståhl, E.; Ceberg, J.; Einhorn, N.; Frödin, J.; Järhult, J.; Lamnevik, G.; Lindholm, C.; The Swedish Council on Technology Assessment in Health Care (SBU) systematic overview of radiotherapy for cancer including a prospective survey of radiotherapy practice in Sweden 2001--summary and conclusions, Acta Oncologica, 2003, 42, 357-365.
4. Jølck, R. I.; Rydhög, J. S.; Christensen, A. N.; Hansen, A. E.; Bruun, L. M.; Schaarup Jensen, H.; von Wenck, A. S.; Børresen, B.; Kristensen, A. T.; Clausen, M. H. Injectable colloidal gold for use in intrafractional 2D image-guided radiation therapy, Adv. Healthcare Mater., 2015, 4, 856-863.
5. Verellen, D.; De Ridder, M.; Storme, G. A (short) history of image-guided radiotherapy, Radiother. Oncol., 2008, 86, 4-13.
6. Giraud, P.; Yorke, E.; Jiang, S.; Simon, L.; Rosenzweig, K.; Mageras, G. Reduction of organ motion effects in IMRT and conformal 3D radiation delivery by using gating and tracking techniques, Cancer Radiothér., 2006, 10, 269-282.
7. Qi, X. S. Image-guided radiation therapy, An Introduction to Medical Physics, Springer 2017, pp. 131-173.
8. Arosio, P.; Avolio, M.; Gargano, M.; Orsini, F.; Gallo, S.; Melada, J.; Bonizzoni, L.; Ludwig,

N.; Veronese, I. Magnetic stimulation of gold fiducial markers used in Image-Guided Radiation Therapy: Evidences of hyperthermia effects, Measurement, 2020, 151, 107242.

9. Fischer-Valuck, B W.; Henke, L.; Green, O.; Kashani, R.; Acharya, S.; Bradley, J. D.; Robinson, C. G.; Thomas, M.; Zoberi, I.; Thorstad, W. Two-and-a-half-year clinical experience with the world's first magnetic resonance image guided radiation therapy system, Adv. Radiat. Oncol., 2017, 2, 485-493.
10. Machiels, M.; van Hooft, J.; Jin, P.; van Berge Henegouwen, M. I.; van Laarhoven, H. M.; Alderliesten, T.; Hulshof, M. C. Endoscopy/EUS-guided fiducial marker placement in patients with esophageal cancer: a comparative analysis of 3 types of markers, Gastrointest. Endsc., 2015, 82, 641-649.
11. Bhagat, N.; Fidelman, N.; Durack, J. C.; Collins, J.; Gordon, R. L.; LaBerge, J. M.; Kerlan, R.K. Complications associated with the percutaneous insertion of fiducial markers in the thorax, Cardiovascular Intervent. Radiol., 2010, 33, 1186-1191.
12. N. Kothary, J.J. Heit, J.D. Louie, W.T. Kuo, B.W. Loo Jr, A. Koong, D.T. Chang, D. Hovsepian, D.Y. Sze, L.V. Hofmann, Safety and efficacy of percutaneous fiducial marker implantation for image-guided radiation therapy, J. Vascular Intervent. Radiol., 2009, 20, 235-239.
13. Loh, J.; Baker, K.; Sridharan, S.; Greer, P.; Wratten, C.; Capp, A.; Gallagher, S.; Martin, J. Infections after fiducial marker implantation for prostate radiotherapy: are we underestimating the risks?, Radiat. Oncol., 2015, 10, 1-5.
14. Fawaz, Z.; Yassa, M.; Nguyen, D.; Vavassis, P. Fiducial marker implantation in prostate radiation therapy: complication rates and technique, Cancer Radiother., 2014, 18, 736-739.
15. Xu, J.; Yu, M.; Carter, P.; Hernandez, E.; Dang, A.; Kapur, P.; Hsieh, J. H.; Zheng, J. In vivo X-ray imaging of transport of renal clearable gold nanoparticles in the kidneys, Angew. Chem. Int. Ed., 2017, 56, 13356-13360.
16. Kim, T.; Lee, N.; Arifin, D. R.; Shats, I.; Janowski, M.; Walczak, P.; Hyeon, T.; Bulte, J. W. In vivo micro-CT imaging of human mesenchymal stem cells labeled with gold-poly-l-lysine nanocomplexes, Adv. Funct. Mater., 2017, 27, 1604213.
17. Ikeda, K.; Liu, H.; Miyamoto, N; Nguyen, M. T.; Shirato, H.; Yonezawa, T. Preparation of Biopex-supported gold nanoparticles as a potential fiducial marker for image-guided radiation therapy, ACS Appl. Bio Mater., 2022, 5, 1259-1265.
18. Narayanan, S.; Sathy, B. N.; Mony, U.; Koyakutty, M.; Nair, S. V.; Menon, D. Biocompatible magnetite/gold nanohybrid contrast agents via green chemistry for MRI and CT bioimaging, ACS Appl. Mater. Interfaces, 2012, 4, 251-260.
19. Ke, H.; Wang, J.; Dai, Z.; Jin, Y.; Qu, E.; Xing, Z.; Guo, C.; Yue, X.; Liu, J. Gold-nanoshelled microcapsules: a theranostic agent for ultrasound contrast imaging and photothermal therapy, Angew. Chem. Int. Ed., 2011, 50, 3017-3021.
20. Li, W.; Chen, X. Gold nanoparticles for photoacoustic imaging, Nanomedicine, 2015, 10, 299-320.
21. Cheng, X.; Sun, R.; Yin, L.; Chai, Z.; Shi, H.; Gao, M. Light-triggered assembly of gold nanoparticles for photothermal therapy and photoacoustic imaging of tumors in vivo, Adv. Mater., 2017, 29, 1604894.
22. Zhang, W.; Ding, X.; Cheng, H.; Yin, C.; Yan, J.; Mou, Z.; Wang, W.; Cui, D.; Fan, C.; Sun, D. Dual-targeted gold nanoprism for recognition of early apoptosis, dual-model imaging and precise cancer photothermal therapy, Theranostics, 2019, 9, 5610.

23. Liu, Y.; Yang, Z.; Huang, X.; Yu, G.; Wang, S.; Zhou, Z.; Shen, Z.; Fan, W.; Liu, Y.; Davisson, M. Glutathione-responsive self-assembled magnetic gold nanowreath for enhanced tumor imaging and imaging-guided photothermal therapy, ACS Nano, 2018, 12, 8129-8137.
24. Sun, W.; Luo, L.; Feng, Y.; Cai, Y.; Zhuang, Y.; Xie, R. J.; Chen, X.; Chen, H. Aggregation-Induced Emission Gold Clustoluminogens for Enhanced Low-Dose X-ray-Induced Photodynamic Therapy, Angew. Chem. Int. Ed., 2020, 59, 9914-9921.
25. Liang, R.; Liu, L.; He, H.; Chen, Z.; Han, Z.; Luo, Z.; Wu, Z.; Zheng, M.; Ma, Y.; Cai, L. Oxygen-boosted immunogenic photodynamic therapy with gold nanocages@ manganese dioxide to inhibit tumor growth and metastases, Biomaterials, 2018, 177, 149-160.
26. Calavia, P. G.; Chambrier, I.; Cook, M. J.; Haines, A. H.; Field, R. A.; Russell, D. A.; Targeted photodynamic therapy of breast cancer cells using lactose-phthalocyanine functionalized gold nanoparticles, J. Colloid Interface Sci., 2018, 512, 249-259.